



Turbulent kinetic energy dissipation rate and associated fluxes in the western tropical Atlantic estimated from ocean glider observations

Peter M. F. Sheehan, Gillian M. Damerell, Philip J. Leadbitter, Karen J. Heywood, and Rob A. Hall

Centre for Ocean and Atmospheric Sciences, School of Environmental Science, University of East Anglia, Norwich, NR4 7TJ, United Kingdom

Correspondence: Peter M. F. Sheehan (p.sheehan@uea.ac.uk)

Received: 19 May 2022 – Discussion started: 31 May 2022

Revised: 5 January 2023 – Accepted: 6 January 2023 – Published: 24 January 2023

Abstract. Ocean gliders enable us to collect the high-resolution microstructure observations necessary to calculate the dissipation rate of turbulent kinetic energy, ε , on timescales of weeks to months: far longer than is normally possible using traditional ship-based platforms. Slocum gliders have previously been used to this end; here, we report the first detailed estimates of ε calculated using the Batchelor spectrum method on observations collected by a FP07 fast thermistor mounted on a Seaglider. We use these same fast thermistor observations to calculate ε following the Thorpe scale method and find very good agreement between the two methods. The Thorpe scale method yields larger values of ε , but the average difference, which is less than an order of magnitude, is smaller than reported elsewhere. The spatio-temporal distribution of ε is comparable for both methods. Maximum values of ε ($10^{-7} \text{ W kg}^{-1}$) are observed in the surface mixed layer; values of approximately $10^{-9} \text{ W kg}^{-1}$ are observed between approximately 200 and 500 m depth. These two layers are separated by a 100 m thick layer of low ε ($10^{-10} \text{ W kg}^{-1}$), which is co-located with a high-salinity layer of Subtropical Underwater and a peak in the strength of stratification. We calculate the turbulent heat and salt fluxes associated with the observed turbulence. Between 200 and 500 m, ε induces downward fluxes of both properties that, if typical of the annual average, would have a very small influence on the heat and salt content of the overlying salinity-maximum layer. We compare these turbulent fluxes with two estimates of double-diffusive fluxes that occur in regions susceptible to salt fingers, such as the western tropical Atlantic. We find that the double-diffusive fluxes of both heat and salt are larger than the corresponding turbulent fluxes.

1 Introduction

Turbulence in the ocean and the mixing of different water masses that it induces are of fundamental importance to ocean dynamics. Over relatively small scales, turbulent mixing often controls the distribution of key water mass properties and tracers; over the world ocean, the sum of these small-scale processes is responsible for the closure of the thermohaline circulation and for the primary production that relies on the upward flux of nutrients to the euphotic zone.

Estimating the dissipation rate of turbulent kinetic energy, ε , from high-resolution observations of shear and temperature (e.g. Lueck et al., 2002; Oakey, 1982; Ruddick et al., 2000) has, historically, required considerable ship time, plus specialist instruments and expertise, so there are relatively few of such estimates. Methods such as Thorpe scaling (Thorpe, 1977) and finescale parameterisation (Polzin et al., 2014; Whalen et al., 2015) have been developed to enable ε to be estimated from standard conductivity–temperature–depth (CTD) and acoustic Doppler current profile (ADCP) observations of temperature, salinity and current velocity – hereafter referred to as finescale methods and observations. Although finescale methods do not require specialist instruments (e.g. Fer et al., 2010b; Whalen et al., 2012, 2015), they are dependent on more assumptions; their results tend not to be valid over as wide a range of conditions as those derived from high-resolution, microstructure-scale observations (Polzin et al., 2014; Whalen, 2021) – hereafter referred to as microstructure methods and observations. Thus, despite the widespread use of finescale methods, the potential remains for discrepancies between estimates of ε based on finescale and microstructure observations (Howatt et al., 2021).

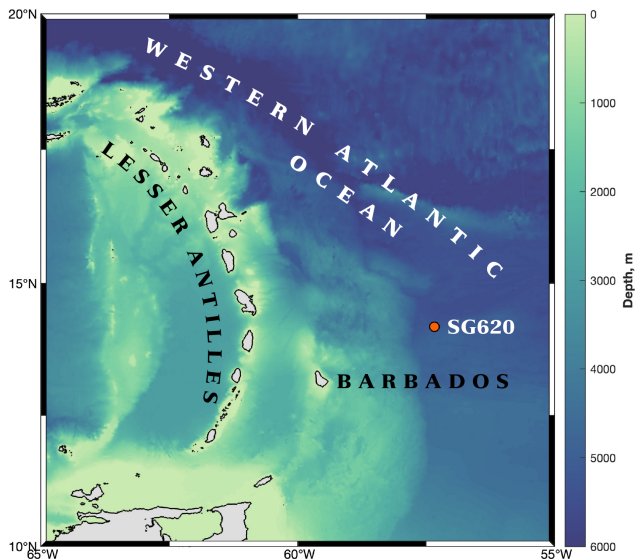


Figure 1. Bathymetry (m) of the western tropical Atlantic and the eastern Caribbean Sea in the region of the Lesser Antilles. The location of SG620, north-east of Barbados, is marked by the orange circle. Land is shaded grey.

Given the proliferation in the use of buoyancy-driven ocean gliders over the last decade, there is growing interest in using them to collect microstructure observations. Because of a glider's smooth flight through the water column, it resembles the free-falling, loosely tethered profilers traditionally used to collect microstructure observations. A growing body of literature makes use of microstructure observations collected by gliders and sets out the best ways of processing such data sets (e.g. Fer et al., 2010b; Peterson and Fer, 2014; Palmer et al., 2015; Schultze et al., 2017; Scheifele et al., 2018; Scott et al., 2021). Up until now, the majority of studies have used microstructure shear observations collected by Slocum gliders (Palmer et al., 2015). Some authors have used microstructure temperature observations to estimate ε (e.g. Peterson and Fer, 2014; Scheifele et al., 2018), while Rainville et al. (2017) briefly discuss the microstructure system developed for use on Seagliders, another commonly used glider platform, and present estimates of the rate of dissipation of temperature variance, χ . However, observational studies of turbulence using autonomous platforms other than Slocum gliders are known to be lacking (Frajka-Williams et al., 2021). Here, we report in detail the first microstructure-based estimates of ε calculated from Seaglider microstructure temperature observations, and we compare the results with estimates of ε calculated by applying the Thorpe scale method, commonly applied to finescale temperature and salinity observations, to the same microstructure observations.

The western tropical Atlantic (Fig. 1) is known for the persistent presence of the salt-fingering regime of double diffusion (Schmitt et al., 1987; Rollo et al., 2022). For salt

fingering to occur, warm, saline water must overlies cooler, fresher water: the water column is therefore stably stratified by temperature but unstably stratified by salinity. Such conditions are maintained in the western tropical Atlantic by the presence of Subtropical Underwater (SUW) at the base of the mixed layer, a warm, high-salinity water mass common to tropical regions (Schmitt et al., 1987; Fer et al., 2010a). Beneath SUW, temperature and salinity both decrease with depth. In a salt-fingering regime, the slow molecular diffusion of salt relative to the fast diffusion of heat leads to the development of salt fingers: narrow, small-scale filaments of alternately upwelling warming water and downwelling cooling water. Over time, double-diffusive convection and salt fingers promote the formation of thermohaline staircases: temperature and salinity profiles characterised by a series of homogeneous mixed layers separated by sharp, narrow gradient layers. Such staircases have previously been observed in the western tropical Atlantic (Schmitt et al., 1987; Rollo et al., 2022). Importantly for studies of ocean mixing, double-diffusive convection enables the vertical transport of heat and salt by a mechanism other than the mechanical, turbulent mixing captured by ε .

Here, we use microstructure temperature observations collected by a Seaglider to estimate ε using the Batchelor spectrum method (Sect. 2.2 herein; Batchelor, 1959) and using the Thorpe scale method (Sect. 2.3 herein; Thorpe, 1977), and we compare the results (Sect. 3.1). From these estimates of ε , we derive turbulent fluxes of heat and salt through an observed layer of elevated ε (Sect. 3.2) and compare these with heat and salt fluxes driven by salt fingers and double-diffusive mixing (Sect. 3.3). We discuss the results in Sect. 4.

2 Data and methods

2.1 Glider observations

As part of the EUREC4A field campaign (Stevens et al., 2021), Seaglider 620 was deployed at 14.2° N, 57.3° W, approximately 200 km north-east of Barbados (Fig. 1) on 23 January 2020. It completed 131 dives to 750 m before being recovered on 5 February 2020. The glider carried an un-pumped conductivity–temperature (CT) sail measuring in situ conductivity and temperature, and a microstructure system. Given the shape of the Seaglider's hull, it is not possible to mount an all-in-one microstructure payload, such as the Rockland Scientific International (RSI) MicroRider that is used on Slocum gliders (e.g. Fer et al., 2014; Schultze et al., 2017; Scheifele et al., 2018). Instead, a reconfigured payload is used, consisting of a pair of RSI MicroPod sensor modules mounted on either side of the CT sail; a dedicated pressure housing containing the system's data logger is mounted inside the Seaglider's aft fairing (Creed et al., 2015). The system draws its power from the Seaglider and can be turned on and off on a dive-by-dive basis.

During the EUREC4A campaign, the glider was equipped with one MicroPod carrying a shear probe and one MicroPod carrying an FP07 fast-response temperature sensor. There was a fault with the shear probe on this deployment, and the observations could not be used. The fast thermistor sensor samples at 512 Hz and has a sensitivity of better than 0.1 mK (Sommer et al., 2013); thermal inertia of the sensor is such that its effective resolution is estimated to be 10 ms (i.e. 100 Hz; Sommer et al., 2013). Microstructure temperature observations are better suited than shear observations to estimating ε in low-dissipation environments (Scheifele et al., 2018) and have the added advantage of being less readily contaminated by platform vibration (Frajka-Williams et al., 2021); here we focus on the temperature-based estimates of ε . The glider’s hydrodynamic flight model, which is used to estimate along-path speed, is tuned following Frajka-Williams et al. (2011), and the thermal lag of the standard CT sail is corrected following Garau et al. (2011).

2.2 Estimating ε using the Batchelor spectrum method

We estimate ε from the glider’s fast thermistor temperature microstructure observations using the Batchelor spectrum method; we hereafter refer to these estimates as ε_μ . For this, we use the MATLAB toolbox produced by Benjamin Scheifele and Jeffrey Carpenter (https://github.com/bscheife/turbulence_temperature, last access: 17 January 2023) and recently used by Howatt et al. (2021). The method is described in detail by Scheifele et al. (2018); much of the underlying theory, as well as a similar methodology, is described by Peterson and Fer (2014), so we here give only an outline.

We divide the temperature time series from the fast thermistor into half-overlapping segments of 32 s length. Within each 32 s segment, we further divide the measurements into fifteen 4 s, half-overlapping sub-segments. From each sub-segment, we calculate a temperature power spectrum, Δ_4 . We then average these 15 Δ_4 to produce 1 power spectrum, Δ_{32} , that is representative of the original 32 s segment. Values of Δ_{32} at high frequencies, where the thermal inertia of the fast thermistor is such that its temporal response is inadequate, are corrected using the transfer function of Sommer et al. (2013). We convert each Δ_{32} from frequency space to wavenumber space (Fig. 2) using the glider’s along-path speed averaged over the same 32 s and assuming the validity of Taylor’s frozen turbulence hypothesis (Scheifele et al., 2018).

We transform each Δ_{32} into a temperature-gradient spectrum, $\Psi = (2\pi k)^2 \Delta_{32}$, which should resemble the Batchelor spectrum, Ψ_B (Batchelor, 1959), the theoretical spectrum that describes temperature-gradient spectra and which is commonly used when calculating ε_μ (e.g. Oakey, 1982; Ruddick et al., 2000; Peterson and Fer, 2014; Scheifele et al., 2018). The Batchelor spectrum is a function of k_B , the Batchelor wavenumber, and of χ , the rate of destruction of tem-

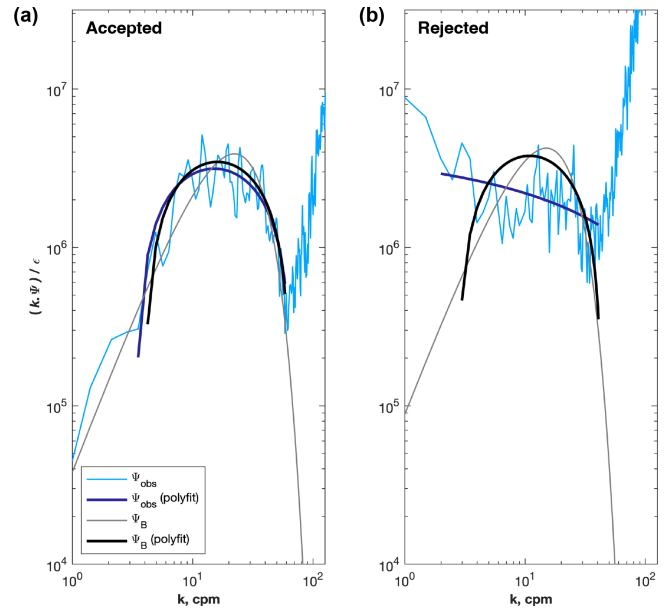


Figure 2. Example of temperature spectra, Ψ , that were accepted (a) and rejected (b) by the quality control algorithm. Observed and theoretical spectra are shown by the thin, light-coloured lines; the second-order polynomial fits are shown by thick, dark-coloured lines.

perature variance (Osborn and Cox, 1972). A comprehensive mathematical treatment of the use of Ψ_B when estimating ε is given by Peterson and Fer (2014). Here, we require k_B in order to calculate ε_μ (W kg^{-1}) according to

$$\varepsilon_\mu = \nu D_T^2 (2\pi k_B)^4, \tag{1}$$

where ν is the kinematic viscosity of seawater, and $D_T = 1.44 \times 10^{-7} \text{ m}^2 \text{ s}^{-1}$ is the molecular diffusion coefficient of temperature.

We calculate χ according to

$$\chi = \chi_1 + \chi_{\text{obs}} + \chi_u$$

$$= 6D_T \left(\int_0^{k_1} \Psi_B dk + \int_{k_1}^{k_u} \Psi dk + \int_{k_u}^{\infty} \Psi_B dk \right), \tag{2}$$

where χ_{obs} is that part of χ derived by integrating Ψ , and χ_1 and χ_u are correction terms derived from Ψ_B . The factor of 6 comes from assuming isotropic turbulence. The wavenumbers k_1 and k_u are, respectively, the lower and upper wavenumber limits of the range over which Ψ is considered reliable; the criteria for choosing k_1 and k_u are explained fully by Scheifele et al. (2018). Given an estimate of χ , the maximum likelihood estimation procedure of Ruddick et al. (2000) is used to find the value of k_B corresponding to the Ψ_B that is the best fit to Ψ between k_1 and k_u . On the first iteration, χ_1 and χ_u are set to zero, and hence $\chi = \chi_{\text{obs}}$. On subsequent iterations, the previous value of χ and the previ-

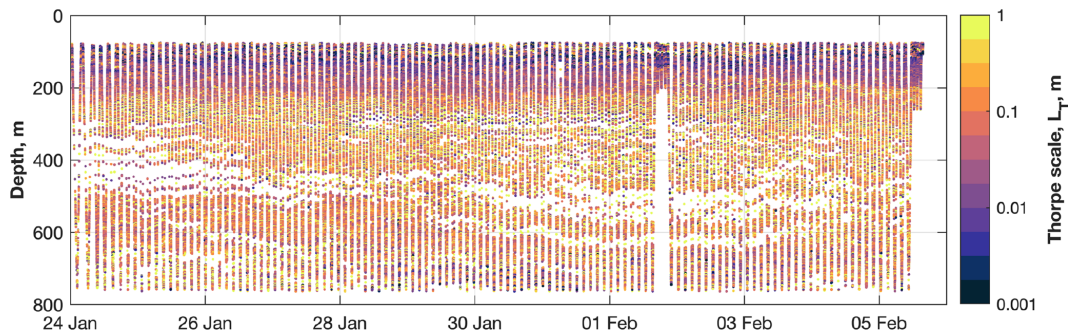


Figure 3. Thorpe scale estimates, L_T (m). Higher values of L_T are indicative of higher dissipation, ε_T .

ous best-fit value of k_B are used to estimate Ψ_B and hence χ_l and χ_u , and the estimate of k_B is further refined.

An observed spectrum that deviates from the shape of the relevant theoretical spectrum should not be used to estimate ε_μ . To discriminate between acceptably and unacceptably shaped spectra, we fit second-order polynomials of the form

$$P(k) = a \cdot \log_{10}(k)^2 + b \cdot \log_{10}(k) + c \quad (3)$$

to both the observed and the theoretical spectra, following the method of Scott et al. (2021), where k is wavenumber, and a , b and c are the polynomial coefficients to be determined. Prior to fitting, we normalise each spectrum by dividing by its corresponding estimate of ε_μ ; this enables the same criteria to be used when assessing goodness of fit over spectra that otherwise span many orders of magnitude. We also multiply spectra by k in order to preserve variance. P is defined over the same range of wavenumbers over which the observed spectrum is integrated when estimating χ .

We accept a spectrum if

1. the value of a fitted to Ψ is positive (note that a fitted to Ψ_B is always positive)
2. the ratio of the a values fitted to Ψ_B and Ψ (a_{Ψ_B}/a_Ψ) is less than 2.

In addition, following Scheifele et al. (2018), we remove an estimate of ε_μ if

3. fewer than six points are included in the spectra fit;
4. the quantity $U/(\varepsilon_\mu/N)^{1/2}$ is less than 5, where U is the glider's speed in the direction of travel, and $(\varepsilon_\mu/N)^{1/2}$ is an estimate of the turbulent flow velocities (Fer et al., 2014), indicating that Taylor's frozen turbulence hypothesis is invalid;
5. the sum of the correction terms χ_u and χ_l is greater than the observed term χ_{obs} (Eq. 2).

Finally, following Peterson and Fer (2014), we remove an estimate of ε_μ if

6. the mean absolute deviation, which quantifies the goodness of fit between Ψ_{obs} and Ψ_B , is greater than $2(2/d)^{1/2}$, where d is the degrees of freedom, calculated as 1.9 multiplied by the number of sub-segments within each 32 s segment, i.e. 1.9×15 ;
7. the estimate of ε_μ is greater than $2 \times 10^{-7} \text{ W kg}^{-1}$ (even having corrected estimates of Δ_{32} at high frequencies, the effective resolution of the fast thermistor, 100 Hz, is such that values of ε_μ greater than this cannot be reliably estimated).

Examples of accepted and rejected spectra are presented in Fig. 2. After quality control, 84 % of ε_μ estimates remained. Quality-controlled estimates of ε_μ were binned, profile by profile, into 25 m vertical bins; we use the geometric mean in preference to the arithmetic (i.e. ordinarily used) mean, as it is better for representing the average of observations that span many orders of magnitude and which are not normally distributed.

2.3 Thorpe scale estimates

We apply the Thorpe scale method (Thorpe, 1977) to the fast thermistor microstructure potential temperature observations to derive a second, independent estimate of the turbulent kinetic energy dissipation rate, hereafter referred to as ε_T . Given that the effective resolution of the fast thermistor is estimated to be 100 Hz, we apply a low-pass, 12th-order Butterworth filter with a cut-off frequency of 100 Hz to remove the highest-frequency variability. This prevents instrumental noise erroneously manifesting as small density overturns (Mater et al., 2015; Ijichi and Hibiya, 2018). Temperature observations were then binned into 10 ms bins using the arithmetic mean, giving an effective vertical resolution of 3 ± 0.5 mm.

Each temperature profile is then re-ordered in depth so that temperature always decreases with depth (i.e. is stable with respect to temperature). From the re-ordered profile we calculate the vertical Thorpe displacement, Δz : the difference between an observation's original depth and its re-ordered depth. We identify an overturn as a vertical segment

in which the cumulative sum of Δz is non-zero and which is bounded above and below by segments in which the cumulative sum of Δz is zero. Following Ijichi and Hibiya (2018) and Howatt et al. (2021), we combine all overturns that are smaller than 2 m and are within 1 m of an adjacent overturn until the region is larger than 2 m. Overturns smaller than 2 m that are farther than 1 m from an adjacent overturn are not aggregated. This assumes that a succession of small overturns is the signal of a once larger, single overturn that has recently decayed into a series of smaller overturns (Smyth et al., 2001). The Thorpe scale, L_T (Fig. 3), is then the root mean square of Δz over an overturn:

$$L_T = \langle \Delta z^2 \rangle^{1/2}, \quad (4)$$

where angular brackets indicate the mean. Larger values of L_T correspond to larger mixing rates; the largest values of L_T (approximately 1 m) are found principally between 200 and 500 m, although much lower values (approximately 0.01 m and lower) are also found within this depth range (Fig. 3). Similarly high values of L_T are also found in the bottom 200 m sampled towards the beginning of the deployment. Above 200 m, values of L_T are much lower, being generally below 0.01 m (Fig. 3).

Finally, we calculate ε_T (W kg^{-1}) from L_T by relating the Ozmidov scale, $L_O = (\varepsilon_T/N^3)^{1/2}$ (Ozmidov, 1965), to L_T by the empirical relation $L_O = 0.8L_T$ (Dillon, 1982), which yields

$$\varepsilon_T = 0.64L_T^2N^3, \quad (5)$$

where N is the background buoyancy frequency calculated using the Seaglider's finescale temperature and salinity observations, binned into 5 m vertical bins, then smoothed in the vertical using a Gaussian-windowed running mean over nine bins (i.e. 45 m).

Our estimates of ε_T are derived from potential temperature rather than potential density; we must therefore assume that temperature is the dominant control on density. In regions where this is not the case – i.e. in regions where salinity is the dominant control on density – temperature perturbations may not correspond to the density perturbations that the Thorpe scale method takes to be indicative of turbulent overturns. To identify regions where salinity is the dominant control on density, we use the density ratio, R_ρ ,

$$R_\rho = \frac{\alpha \Theta_z}{\beta S_z}, \quad (6)$$

where α is the thermal expansion co-efficient, Θ_z is the vertical temperature gradient, β is the haline contraction coefficient, and S_z is the vertical salinity gradient. We calculate Θ_z and S_z from finescale glider observations binned into 5 m vertical bins using the arithmetic mean and find R_ρ at the depth of each overturn. Where $-1 < R_\rho < 1$, salinity is the dominant control on density, and we discard any overturns

and associated value of ε_T . In total, 2388 overturns are discarded by the R_ρ quality control criterion, 4.03 % of the total. In the majority of the water column, temperature is the dominant control on density, and so temperature observations may be reliably used to estimate ε . Estimates of ε_T that are discarded correspond principally to large values of L_T (> 1 m) in mid-depth regions (i.e. between 200 and 600 m). This is the part of the water column in which the majority of the thermohaline staircases are found (Rollo et al., 2022).

Finally, we discard all values of ε_T shallower than 75 m because a temperature inversion in the mixed layer is erroneously identified as an overturn. Remaining estimates of ε_T are binned into 25 m vertical bins using the geometric mean, as for ε_μ .

3 Results

3.1 Estimates of ε

The water masses observed are typical of the region (e.g. Schmitt et al., 1987). A warm ($> 26^\circ\text{C}$) surface mixed layer of intermediate salinity overlies SUW, a salinity-maximum ($> 37.6 \text{ g kg}^{-1}$) layer located in the upper thermocline (Fig. 4). Beneath SUW, temperature and salinity steadily decrease with depth into the Antarctic Intermediate Water layer that lies beneath (Fig. 4). Two maxima in buoyancy frequency are observed: an upper maximum at the base of the surface isohaline layer and a lower maximum at the base of the surface isothermal layer (Fig. 4).

There is generally good agreement between ε_μ and ε_T . Histograms of the two distributions are very similar, and, when scattered one against the other, the points are clustered around the one-to-one line (Fig. 6a and b). The principal difference is at depths between 400 and 600 m in the first 2 d of the deployment, when ε_μ ($> 10^{-9} \text{ W kg}^{-1}$) is noticeably higher than ε_T ($< 10^{-10} \text{ W kg}^{-1}$; Fig. 5). This is a region with a clear pattern in the differences between ε_μ and ε_T : in many other regions, the differences are fairly randomly distributed (Fig. 5c).

Of the two estimates of ε , the higher of the two is ε_T , the geometric mean of which is $3.42 \times 10^{-9} \text{ W kg}^{-1}$; the geometric mean of ε_μ is $3.05 \times 10^{-9} \text{ W kg}^{-1}$. We note that, on average, the difference between the two estimates is small and much less than an order of magnitude. The more variable of the two is ε_μ , the geometric standard deviation factor (GSDF) of which is 5.58. The GSDF of ε_T is 4.43. (Note that GSDF is multiplicative, not additive, and is therefore dimensionless. The range is from the geometric mean/GSDF to geometric mean \times GSDF.) Averages and GSDFs are calculated from bins only where estimates of both ε_μ and ε_T are available.

The highest values of ε are found in approximately the top 50 m of the water column, in the surface mixed layer above the upper boundary of SUW ($> 10^{-8}$; Fig. 5; ε_μ only). The

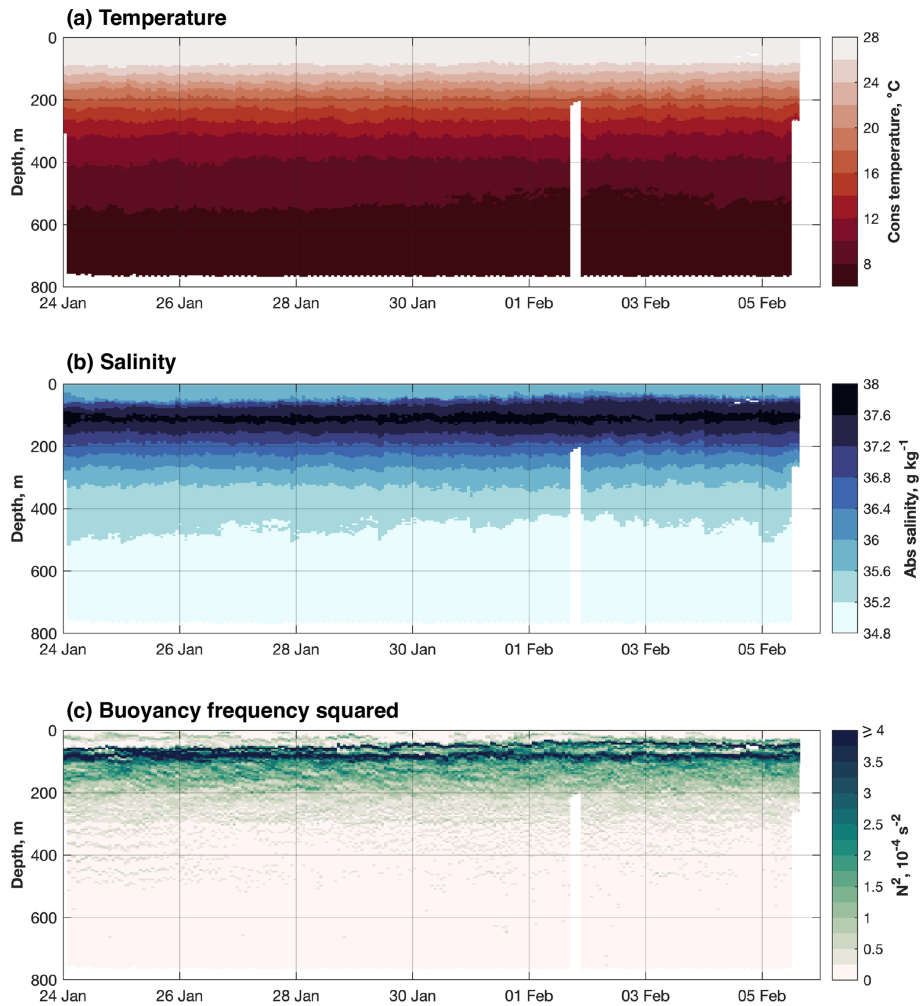


Figure 4. Time series of hydrographic observations from SG620, averaged (arithmetic mean) into 5 m bins: (a) conservative temperature ($^{\circ}\text{C}$), (b) absolute salinity (g kg^{-1}) and (c) buoyancy frequency squared (N^2 ; s^{-2}).

upper boundary of SUW corresponds to the shallowest band of high buoyancy frequency (Fig. 4); a peak in the strength of the stratification might be expected to arrest the downward penetration of surface mixing. But these highest values are infrequently observed: a large proportion of ε_{μ} estimates in the mixed layer are greater than 2×10^{-7} , beyond the range for which the FP07 fast thermistor observations and the Batchelor spectrum method yield meaningful results (Sect. 2.2 herein; Peterson and Fer, 2014). Consequently, the remaining values are all below this threshold; indeed, considerable variability in ε_{μ} is observed in the mixed layer – this is reflected in the relatively high GSDF for ε_{μ} in this region (Fig. 5) – and many remaining estimates are low ($< 10^{-10}$). The mean ε_{μ} in the upper water column is therefore likely to be biased towards these low values. In the remainder of the water column, ε_{μ} and ε_T are predominantly below 2×10^{-7} (Fig. 5); hence the comparison between the two is meaningful.

Between approximately 100 and 200 m, a thin layer with moderate values of ε lies within SUW in the upper thermocline (Figs. 4 and 5). Here, values of both ε_{μ} and ε_T are commonly between $10^{-9.5}$ and $10^{-9} \text{ W kg}^{-1}$. Below this low- ε SUW layer, between approximately 200 and 500 m, is a relatively thick layer with higher values of ε ($10^{-9} < \varepsilon < 10^{-8} \text{ W kg}^{-1}$; Fig. 5). Values of ε_T in this layer are generally higher than values of ε_{μ} (Fig. 5), which would explain why the distribution of ε_T is slightly skewed to higher values than the distribution of ε_{μ} (Fig. 6a). A few values of ε_T are in excess of $10^{-7.5} \text{ W kg}^{-1}$ (Fig. 5). The thickness of this higher- ε_{μ} and higher- ε_T layer increases by 50 to 100 m over the course of the deployment. Below 700 m, both ε_{μ} and ε_T are less than $10^{-10} \text{ W kg}^{-1}$ between 28 January and 4 February; the differences between the two estimates also tend to be lower within this spatio-temporal range (Fig. 5c). This is in contrast to higher values of ε_{μ} and ε_T ($> 10^{-10} \text{ W kg}^{-1}$) within the 700 to 800 m depth range at the beginning and end of the deployment.

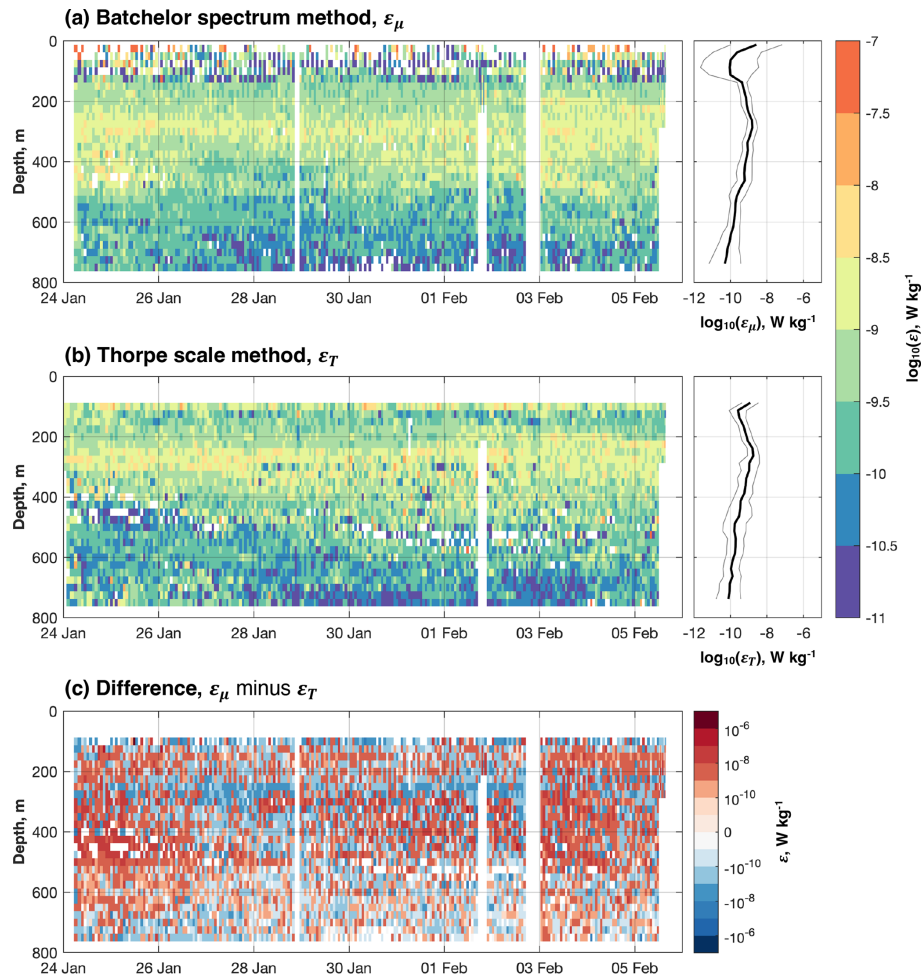


Figure 5. Turbulent kinetic energy dissipation rate, ε (W kg^{-1}), as estimated using (a) the Batchelor spectrum method (ε_{μ}) and (b) the Thorpe scale method (ε_T). The respective geometric means (thick lines) and geometric standard deviation factors (thin lines) are shown in the panels on the right. Note that geometric standard deviation factor is multiplicative. (c) The difference between ε_{μ} and ε_T .

3.2 Heat and salt fluxes

We calculate diapycnal diffusivity, κ_{ρ} , from ε using the Osborn relation:

$$\kappa_{\rho} = \Gamma \frac{\varepsilon}{N^2}, \quad (7)$$

where Γ is mixing efficiency, which is here taken to be 0.2 (Osborn, 1980). We use ε_{μ} in preference to ε_T because the former has better coverage in the mixed layer (Fig. 5).

Below approximately 250 m, the distribution of κ_{ρ} resembles that of ε_{μ} due to the relatively low variability in N^2 at these depths (Fig. 4c). Above 200 m, N^2 increases substantially in the pycnocline, and thus κ_{ρ} decreases. Beneath the surface mixed layer, κ_{ρ} is highest between 400 and 500 m ($< 10^{-4.5} \text{ m}^2 \text{ s}^{-1}$; Fig. 7a), with low values predominating in the core of the high-salinity SUW ($< 10^{-6} \text{ m}^2 \text{ s}^{-1}$; Fig. 7a).

Vertical turbulent heat and salt fluxes, Q_h (W m^{-2}) and Q_S ($\text{kg m}^{-2} \text{ s}^{-1}$), respectively, can be calculated from κ_{ρ} :

$$Q_h = -\rho C_p \kappa_{\rho} \Theta_z \quad (8)$$

$$Q_S = \frac{1}{1000} (-\rho \kappa_{\rho} S_z), \quad (9)$$

where ρ is density, C_p is the specific heat capacity of seawater, Θ_z is the vertical gradient of conservative temperature, and S_z is the vertical gradient of absolute salinity.

Beneath the surface mixed layer, both Q_h and Q_S are predominantly negative (i.e. downward) because temperature and salinity decrease with depth (Fig. 4a and b). The most prominent feature of the distributions of both is the broad region of negative (i.e. downward) turbulent heat and salt transport between approximately 200 and 500 m (Fig. 7b and c). This corresponds to the elevated values of κ_{ρ} ($> 10^{-5} \text{ m}^2 \text{ s}^{-1}$) found within the same depth range (Fig. 7a). Within the surface mixed layer, notwithstanding the limited coverage of the observations, Q_h is positive in the top 50 m

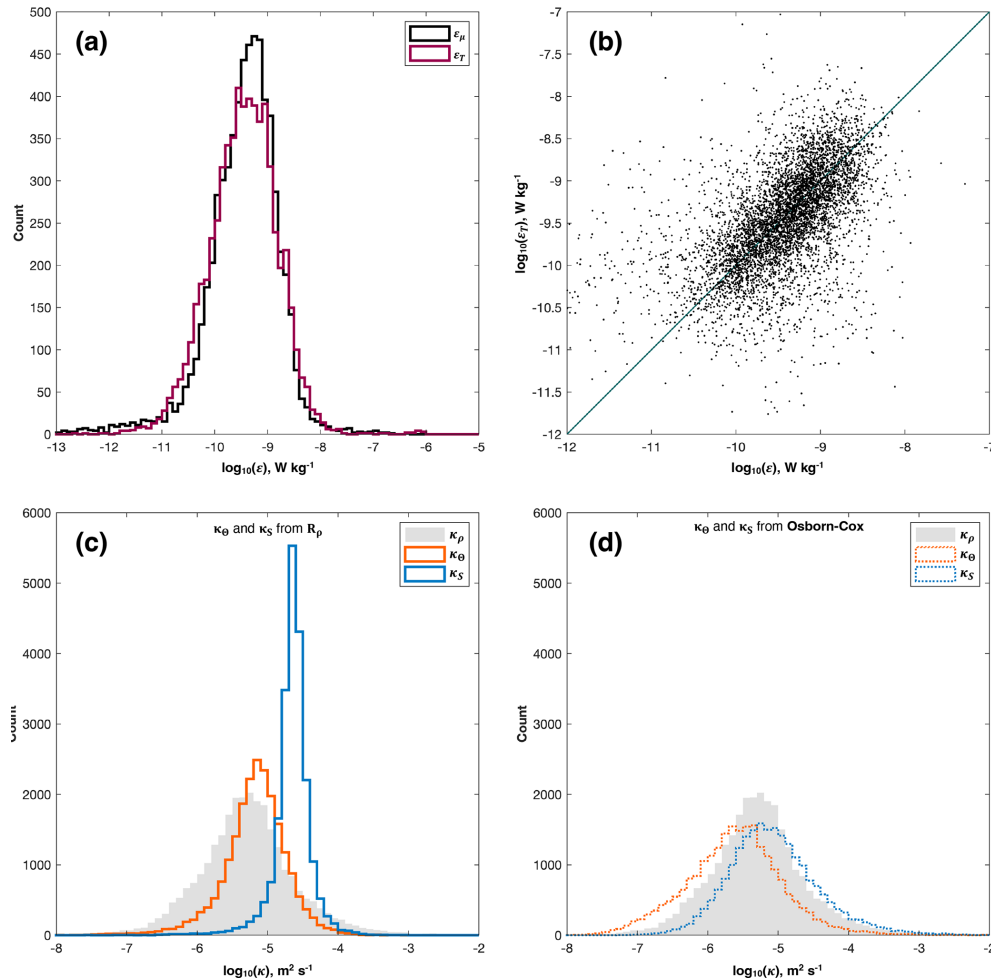


Figure 6. (a) Histograms of turbulent kinetic energy dissipation rate as estimated using the Batchelor spectrum method (ε_{μ} ; green line) and the Thorpe scale method (ε_T ; purple line) (both W kg^{-1}). (b) Scatter plot of ε_T against ε_{μ} . The one-to-one line is shown in dark green. (c) Histograms of thermal diffusivity (κ_{Θ} ; orange line) and haline diffusivity (κ_S ; blue line) as estimated from the density ratio, R_{ρ} . Diffusivity, κ_{ρ} , estimated from the Osborn relation and ε_{μ} , is plotted as the shaded grey histogram. (d) Histograms of κ_{Θ} (dotted orange line) and κ_S (dotted blue line) as estimated from χ using the Osborn–Cox relation. Diffusivity estimated from the Osborn relation is plotted as the shaded grey histogram, as in (c).

and negative between 50 and 100 m; Q_S is positive throughout the surface mixed layer (Fig. 7b and c). This is due to weak thermal and haline inversions near the surface; the depths of the temperature and salinity maxima are indicated by the black lines in Fig. 7b and c, respectively.

We now focus on the 200 to 500 m depth range, the region of highest κ_{ρ} and, consequently, the region in which Q_h and Q_S are most pronounced. Over the period of the observations, the arithmetic mean Q_h between 200 and 500 m was -1.40 W m^{-2} . This and all subsequent flux estimates are summarised in Table 1. The arithmetic mean Q_S between 200 and 500 m was $-5.84 \times 10^{-8} \text{ kg m}^{-2} \text{ s}^{-1}$. This is a relatively low-turbulence region; the attendant turbulent fluxes are correspondingly relatively small and likely have little influence on the region’s hydrography. For instance, integrated over a year, Q_h results in an annual turbulent heat flux of

$-4.43 \times 10^7 \text{ J m}^{-2}$, which would reduce the temperature of the overlying SUW layer (assumed to be 100 m thick) by just $0.11 \text{ }^{\circ}\text{C}$. Similarly integrated over a year, Q_S results in an annual turbulent salt flux of -1.84 kg m^{-2} , which would reduce the salinity of the overlying SUW layer by just 0.02 g kg^{-1} .

3.3 Salt fingers and associated fluxes

Diffusivity as estimated using the Osborn relation, κ_{ρ} , (Eq. 7) and the associated fluxes presented above are derived from ε and so are applicable to transports of heat and salt that are driven by turbulent, mechanical mixing (turbulent regime). However, these ε -based estimates do not account for the fluxes driven by the salt fingers (i.e. double-diffusive mixing; salt-finger regime) that are characteristic of the thermohaline staircases prominent in the western tropical Atlantic

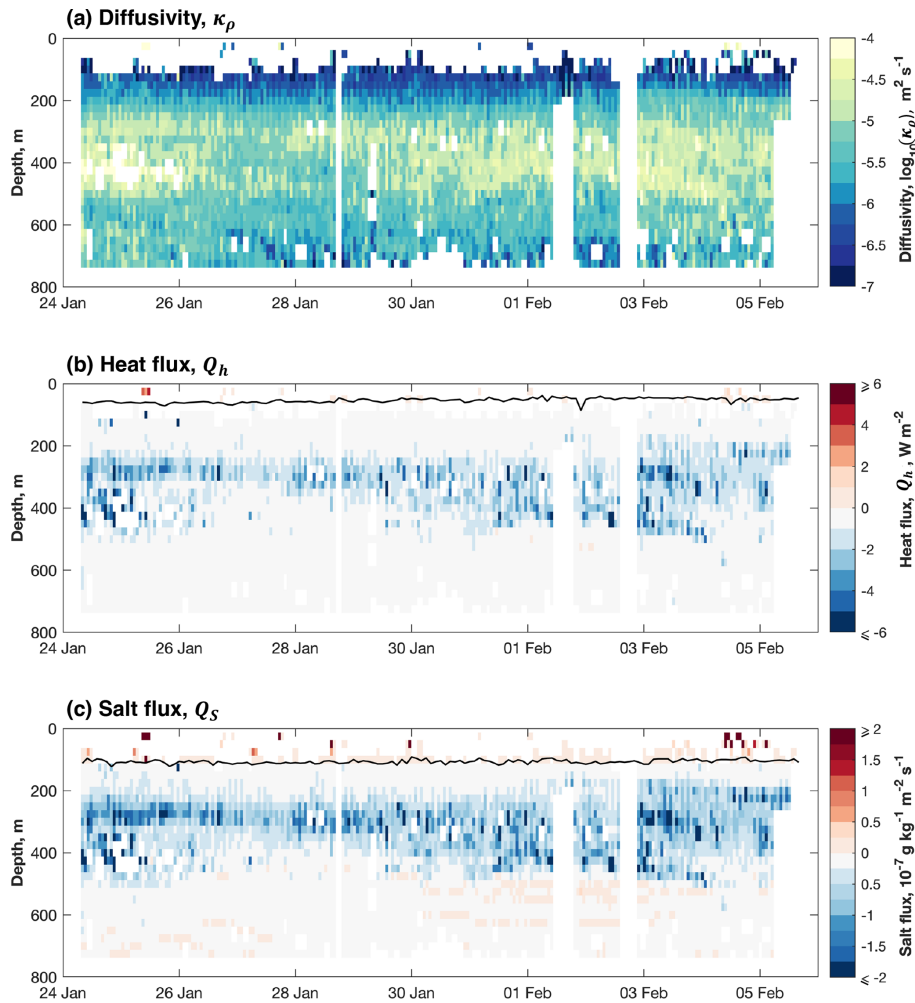


Figure 7. (a) Diffusivity, $\log_{10}(\kappa_\rho)$ ($\text{m}^2 \text{s}^{-1}$). (b) Vertical heat flux, Q_h (W m^{-2}). (c) Vertical salt flux, Q_S ($10^{-7} \text{g kg}^{-1} \text{m}^{-2} \text{s}^{-1}$). Negative fluxes are downward. All are calculated from ε using the Batchelor spectrum method. The black lines in (b) and (c) indicate the depth of, respectively, the temperature and salinity maxima, as derived from 1 m binned Seaglider observations.

(Schmitt et al., 1987; Rollo et al., 2022); Seaglider 620 was deployed at the edge of the region identified by Schmitt et al. (1987) as being the location of strong staircase structures. Such structures are prominent in the temperature observations (Fig. 8). In the turbulent regime, thermal diffusivity, κ_Θ , and haline diffusivity, κ_S , are the same. But in the salt-finger regime, κ_S may be approximately twice κ_Θ ; hence they shall hereafter be considered separately. Moreover, in low-turbulence regions, such as that of the present study, salt fingers give rise to fluxes of heat and salt that can be larger than those driven by mechanical turbulence (Schmitt, 1988).

Those regions of the water column that are susceptible to salt fingers may be identified using the Turner angle, Tu : salt fingers can occur where $45^\circ < Tu < 90^\circ$. The following equations are applied only where this condition is met. Tu is calculated from temperature and salinity binned into 5 m vertical bins; all subsequent diffusivities are calculated from variables binned into 5 m vertical bins in order to match Tu .

We compare two different estimates of κ_Θ and κ_S in the salt-finger regime. Firstly, and given that theoretical flux laws can overestimate κ_S in the real ocean (e.g. Taylor and Veronis, 1996; Kelley et al., 2003; Radko, 2005), we follow van der Boog et al. (2021) in using the empirical relations of Radko and Smith (2012) to calculate κ_Θ and κ_S from the density ratio, R_ρ (Eq. 6), and the molecular diffusivity of heat, K , estimated from temperature and salinity at each grid point:

$$\kappa_S = \left(\frac{135}{(R_\rho - 1)^{1/2}} - 62.75 \right) K R_\rho. \quad (10)$$

From κ_S , again following van der Boog et al. (2021) and Radko and Smith (2012), we then calculate κ_Θ :

$$\kappa_\Theta = \kappa_S \frac{\gamma}{R_\rho}, \quad (11)$$

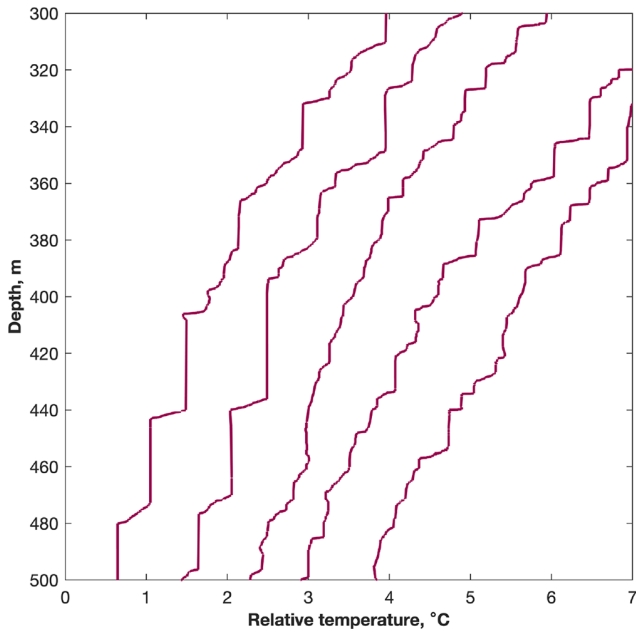


Figure 8. A selection of temperature profiles (presented as relative conservative temperature; °C) recorded by the FP07 fast thermistor. Thermohaline staircases are visible at a variety of scales.

where $\gamma = 2.709e^{-2.513R_\rho} + 0.5128$ is the density flux ratio in the presence of salt fingers. We refer to these salt-finger diffusivities as κ_Θ and κ_S from R_ρ (Fig. 9a and b).

Secondly, we use the Osborn and Cox (1972) relation to estimate κ_Θ and κ_S using χ (Eq. 2; see also St Laurent and Schmitt, 1999; Schmitt et al., 2005; Ijichi and Hibiya, 2018), which we calculated as an intermediary step in the calculation of ε_μ (Sect. 2.2):

$$\kappa_\Theta = \frac{\chi}{2\Theta_z^2}. \quad (12)$$

The relationship between κ_Θ and κ_S when calculated from χ remains as in Eq. (11) (Schmitt et al., 2005; van der Boog et al., 2021). We refer to these second salt-finger diffusivities as Osborn–Cox κ_Θ and κ_S ; we note that the Osborn–Cox relation can include a contribution of mechanical mixing to χ and hence on κ_Θ .

There is approximately an order-of-magnitude difference between κ_Θ and κ_S from R_ρ , the latter being the greater (Figs. 6c and 9a and b). Neither distribution exhibits the same pronounced structure as κ_ρ (Fig. 7a): whereas κ_ρ resembles the distribution of ε_μ , from which it was derived (Fig. 5a) – i.e. with elevated values between 200 and 500 m, and lower values below and, in particular, immediately above – values of κ_Θ and κ_S from R_ρ are relatively constant in depth and time. Of the two, κ_S is the larger, being generally greater than $10^{-4.5} \text{ m}^2 \text{ s}^{-1}$; κ_Θ is generally between 10^{-6} and $10^{-5} \text{ m}^2 \text{ s}^{-1}$, although some values higher than this are present (Figs. 6c and 9a and b). Estimates of both κ_Θ and κ_S from R_ρ are higher than estimates of κ_ρ at the same depth

(Figs. 7a and 9a and b), indicating that the vertical mixing of properties in the salt-finger regime is higher than in the turbulent regime.

We then substitute κ_Θ from R_ρ (Fig. 9a) into Eq. (8) in place of κ_ρ (Fig. 7a). Averaged (arithmetic mean) between 200 and 500 m, κ_Θ from R_ρ gives rise to a heat flux of -1.71 W m^{-2} in the salt-finger regime (Table 1), an annual temperature reduction of $0.13 \text{ }^\circ\text{C}$ in the SUW layer. This flux is larger than the value reported above for the turbulent regime (Sect. 3.2). Similarly, we substitute κ_S from R_ρ (Fig. 9b) into Eq. (9) in place of κ_ρ . Averaged (arithmetic mean) between 200 and 500 m, κ_S from R_ρ gives rise to a salt flux of $-1.83 \times 10^{-7} \text{ kg m}^{-2} \text{ s}^{-1}$ in the salt-finger regime (Table 1), or an annual reduction of 0.06 g kg^{-1} in the salinity of the SUW layer. This flux is over 3 times larger than the corresponding salt flux in the turbulent regime. Note that, for the calculation of the arithmetic mean heat and salt fluxes in the salt-finger regime, we set both κ_T and κ_S from R_ρ to zero outside of the salt-finger regimes, i.e. where $Tu < 45^\circ$ and $Tu > 90^\circ$, and include these zeros in our averages. Because we first filter out regions of the water column that are not susceptible to salt fingering, gaps in the record therefore indicate an absence of the process to be averaged (i.e. salt-finger-driven fluxes) rather than an absence of data.

The distributions of κ_Θ and κ_S from the Osborn–Cox relation resemble the distribution of ε , which itself resembles the distribution of χ that was used to calculate both diffusivities (not shown): the highest diffusivities are found between 200 and 500 m, with lower values being found above and below. In both cases, the highest diffusivities are between 10^{-6} and $10^{-5} \text{ m}^2 \text{ s}^{-1}$; within this range, κ_S is greater (Figs. 6d and 9c and d). Above and below this depth range, κ_Θ decreases to values below $10 \times 10^{-6.5} \text{ m}^2 \text{ s}^{-1}$ (Fig. 9c), whereas κ_S decreases only to values of approximately $10^{-5.5} \text{ m}^2 \text{ s}^{-1}$ (Fig. 9c).

We then substitute κ_Θ from the Osborn–Cox relation (Fig. 9c) into Eq. (8) in place of κ_ρ . Averaged (arithmetic mean) between 200 and 500 m, κ_Θ from the Osborn–Cox relation gives rise to a heat flux of -1.49 W m^{-2} in the salt-finger regime (Table 1), an annual temperature reduction of $0.11 \text{ }^\circ\text{C}$ in the SUW layer. This heat flux is very similar to that reported for the turbulent regime and less than that predicted by the empirical relation of Radko and Smith (2012) reported above (i.e. κ_Θ and κ_S from R_ρ). And κ_S , averaged (arithmetic mean) between 200 and 500 m, gives rise to a salt flux of $-9.40 \times 10^{-8} \text{ kg m}^{-2} \text{ s}^{-1}$ (Table 1), an annual salinity reduction of 0.03 g kg^{-1} in the SUW layer. This flux is approximately 1.6 times that reported for the turbulent regime, but half that predicted by the empirical relation of Radko and Smith (2012). As before, we set both κ_T and κ_S from the Osborn–Cox relation to zero outside of the salt-finger regimes.

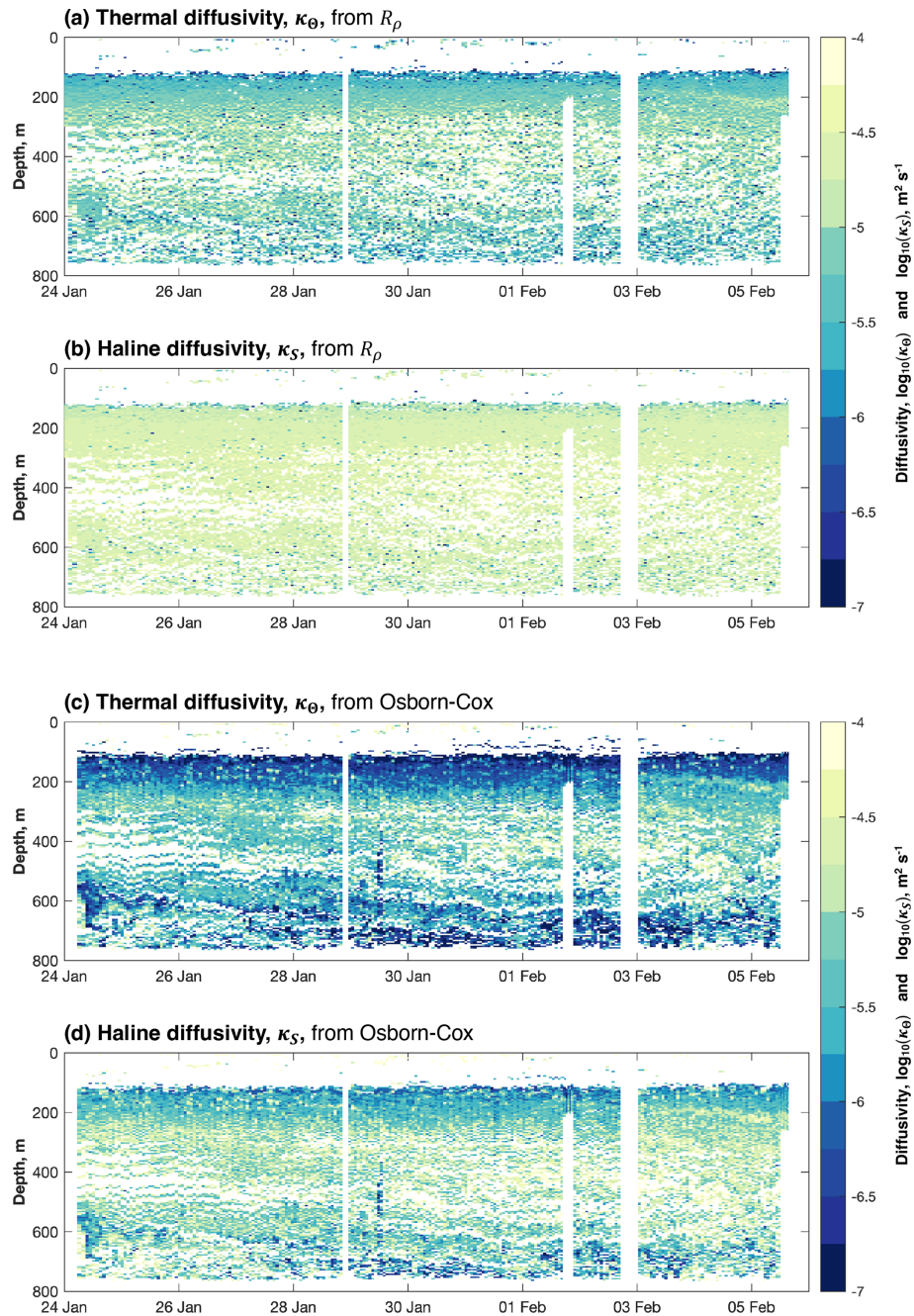


Figure 9. (a) Thermal diffusivity, κ_{θ} , and (b) haline diffusivity, κ_S (both $\text{m}^2 \text{s}^{-1}$), in the presence of salt fingers as calculated from the density ratio, R_{ρ} , and the molecular diffusivity of heat, K , following van der Boog et al. (2021). (c) κ_{θ} and (d) κ_S in the presence of salt fingers as calculated from our estimates of χ using the Osborn–Cox relation (Sect. 2.2 herein; Osborn and Cox, 1972). Diffusivities are plotted only in regions of the water column susceptible to salt fingers, i.e. where the Turner angle is between 45 and 90° .

4 Discussion

4.1 Comparing ε_{μ} and ε_T

Our finding that estimates of ε_T are higher than estimates of ε_{μ} is in agreement with the findings of Howatt et al. (2021). They report that, while the Thorpe scale method can well

represent qualitative aspects of the spatio-temporal distribution of ε , the method can, when applied to relatively low-resolution, finescale observations, artificially inflate ε_T by an order of magnitude relative to estimates from, for instance, the Batchelor spectrum method. This is for the simple reason that finescale observations lack the resolution to capture

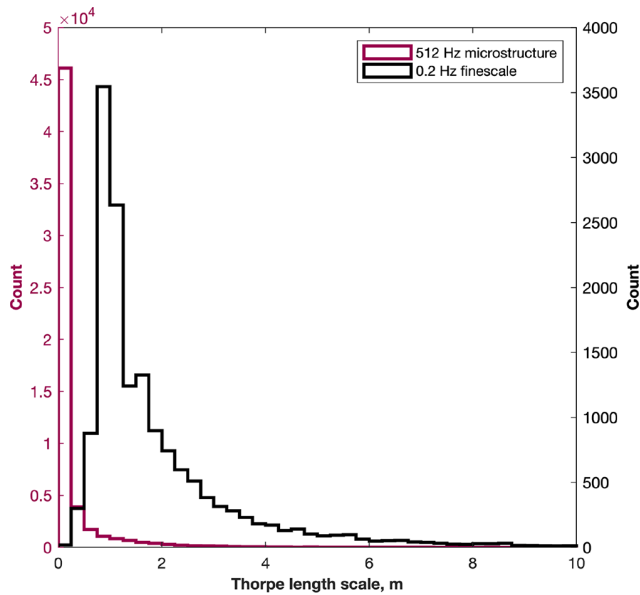


Figure 10. Histograms of Thorpe scale, L_T , as calculated from FP07 microstructure observations (purple line; left-hand axis) and ordinary Seaglider finescale observations (black line; right-hand axis).

small-scale overturns; the resultant distribution of L_T , and hence of ε , is consequently biased towards high values.

This is supported by our observations: the differences between ε_μ and ε_T reported here are much lower, being, on average, far less than an order of magnitude (Sect. 3, Figs. 5 and 6). Further, we directly compare L_T calculated using the FP07 microstructure observations (512 Hz, 100 Hz when accounting for the sensor's response time; Fig. 3) to L_T calculated using the Seaglider's ordinary finescale temperature and salinity observations (0.2 Hz). The distribution of L_T derived from microstructure observations has a pronounced peak at very low values (> 0.25 m; Fig. 10). In contrast, the finescale glider observations are unable to resolve values of L_T at this scale (Fig. 10). The better agreement between ε_μ and ε_T reported here than by Howatt et al. (2021) therefore appears to be explained by the higher vertical resolution of our observations. Consequently, and in agreement with Howatt et al. (2021), we suggest that, in a low-turbulence environment, the Thorpe scale method is unable to produce reliable quantitative estimates of ε unless it is applied to microstructure observations. In a high-turbulence environment where overturns are large, finescale observations may be better able to accurately resolve the distribution of L_T , and their relatively low resolution may not introduce such a systematic bias.

A potential problem with using the Thorpe scale method on Seaglider observations is the non-vertical profile that the Seaglider collects: unlike, for instance, a ship-deployed CTD or a vertical microstructure profiler, a Seaglider follows a slanted trajectory, typically covering a horizontal distance

Table 1. Heat and salt flux estimates calculated using diffusivities in the turbulent and salt-finger regime. Fluxes for the latter regime are estimated from R_ρ using the empirical relations of Radko and Smith (2012) and from χ using the Osborn–Cox relation (Osborn and Cox, 1972). All flux estimates have been averaged (arithmetic mean) between 200 and 500 m.

Regime	Heat flux, Q_h (W m^{-2})	Salt flux, Q_S ($\text{kg m}^{-2} \text{s}^{-1}$)
Turbulent	−1.40	$−5.84 \times 10^{-8}$
Salt finger, R_ρ	−1.71	$−1.83 \times 10^{-7}$
Salt finger, Osborn–Cox	−1.49	$−9.40 \times 10^{-8}$

of 4 km over a 1000 m deep dive–climb cycle. Any resultant sampling of horizontal gradients, particularly in the presence of internal waves, could artificially inflate estimates of ε_T due to false overturn detection (Thorpe, 2012). However, this is a concern only when the internal wave slope exceeds the slope of the Seaglider's trajectory. Following Howatt et al. (2021), we calculate that the mean (± 1 standard deviation) of SG620's trajectory slope (from the horizontal) during the Eurec4a deployment was 0.70 ± 0.09 , i.e. greater than the upper limit of the slope of internal waves (approximately 0.3; Thorpe, 1978; Howatt et al., 2021). Consequently, false overturn detection due to the Seaglider's sloping trajectory is unlikely to lead to overestimation of ε_T in this data set.

4.2 Observed dissipation in spatial and temporal context

Values of ε in the western tropical Atlantic are broadly consistent with other open-ocean regions away from shallow topography. For instance, Sheen et al. (2013) and Naveira Garabato et al. (2016) report background ε values of approximately 10^{-10} to $10^{-9} \text{ W kg}^{-1}$ downstream of the Drake Passage, with values in excess of $10^{-8} \text{ W kg}^{-1}$ in the upper 1000 m and in the vicinity of rough topography. George et al. (2021) report ε values between 10^{-10} and $10^{-8} \text{ W kg}^{-1}$ in the upper layers of the south-western Bay of Bengal. And Peterson and Fer (2014) report mission-mean values of between 10^{-8} and $10^{-7} \text{ W kg}^{-1}$ from observations collected near the Faroe Islands in the northern Atlantic.

Limited estimates of ε are available for the western tropical Atlantic. Two profiles from the region, collected by a microstructure turbulence profiler, were presented by Fernández-Castro et al. (2014). Similarly to our profiles, they find surface ε values between approximately 10^{-7} and $10^{-6} \text{ W kg}^{-1}$ and values between approximately 10^{-9} and $10^{-8} \text{ W kg}^{-1}$ between 50 and 300 m. Below 50 m, their estimates of κ_ρ are similar to ours, although they report near-surface values several orders of magnitude larger than ours (e.g. $> 10^{-3} \text{ m}^2 \text{ s}^{-1}$). Our methods do not yield reliable estimates of high turbulence in the mixed layer, however, so a full comparison is not possible. Two sets of observations

taken several years apart and separated by up to hundreds of kilometres cannot be readily compared; moreover, their profiles do not extend deeper than 300 m. Interannual variability and geographic differences could be pronounced. Nevertheless, there is no evidence in their deepest observations of an increase in ε that might indicate the presence of the elevated- ε layer that we observe beneath SUW (Figs. 4 and 5) and which, to our knowledge, has not previously been described.

4.3 Diffusivity and its influence on hydrography

The distribution of κ_{Θ} and κ_S from the Osborn–Cox relation (i.e. from χ) resembles that of κ_{ρ} – itself derived from ε_{μ} – far more closely than do either κ_{Θ} or κ_S from R_{ρ} (Figs. 7a and 9). Notably, neither κ_{Θ} nor κ_S from R_{ρ} seems to be particularly influenced by features of the water column that might be expected to influence vertical diffusivity, such as stratification (Fig. 4c) or temperature and salinity gradients (not shown). Given that the Osborn–Cox relation explicitly relates diffusivity to a mixing variable (i.e. χ), we suspect that it is more accurate than the empirical relation of Radko and Smith (2012), i.e. κ_{Θ} and κ_S from R_{ρ} .

As calculated from R_{ρ} (Radko and Smith, 2012), heat flux due to salt fingers is 1.22 times greater than that due to turbulent mixing; as calculated from χ (Osborn and Cox, 1972), the heat flux due to salt fingers is 1.06 times that due to turbulent mixing. And as calculated from R_{ρ} , the salt flux due to salt fingers is 3.31 times greater than that due to turbulent mixing; as calculated from χ , the salt flux due to salt fingers is 1.6 times that due to turbulent mixing. In all instances, heat and salt fluxes due to salt fingers (i.e. double-diffusive convection) are higher than turbulent fluxes. The empirical relations of Radko and Smith (2012) predict a relatively large difference, whereas the Osborn–Cox relation predicts a difference that is relatively small – indeed, for heat, the turbulent and salt-finger fluxes are almost the same. The choice of equation used to calculate diffusivities in the salt-finger regime makes a considerable difference to the result.

The dissipation rates and diffusivities presented above appear to have a limited influence on the hydrography of the study region. If the turbulent fluxes estimated above are representative of annual average conditions, heat and salt from the SUW layer penetrate downwards into the ocean interior relatively slowly; over the 12 d of the Eurec4a Seaglider deployment, the hydrographic influence of the fluxes would be negligible. As calculated from R_{ρ} , the double-diffusive heat flux due to salt fingers is 1.2 times greater than that due to turbulent mixing; as calculated from χ the double-diffusive heat flux due to salt fingers is the same as that due to turbulent mixing. Salt fingers potentially have a greater influence on hydrography than turbulent mixing, but the overall effect would still be nearly inconsequential.

5 Conclusions

We demonstrate that microstructure temperature observations collected by a Seaglider-mounted FP07 fast thermistor may be used to estimate the dissipation rate of turbulent kinetic energy, ε . We estimate ε using the Batchelor spectrum method (ε_{μ}) and the Thorpe scale method (ε_T). The results from the two methods agree well, although ε_T is on average higher than ε_{μ} . This is in agreement with previous studies, although the difference reported here, which is less than an order of magnitude, is below that reported elsewhere. This improved agreement is due to ε_T being calculated using the same high-resolution observations as were used to calculate ε_{μ} : other studies (e.g. Howatt et al., 2021) have compared ε_{μ} to ε_T calculated using lower-resolution, finescale temperature observations that are unable to resolve overturns below a certain size, thus biasing estimates of ε towards high values.

We identify a layer of elevated ε values between 200 and 500 m that lies immediately below Subtropical Underwater, a high-salinity sub-surface water mass that is co-located with a maximum in stratification. We estimate that, over the period of the deployment, this elevated- ε layer is responsible for a mean heat flux of -1.40 W m^{-2} and a mean salt flux of $-5.84 \times 10^{-8} \text{ kg m}^{-2} \text{ s}^{-1}$. Given the prevalence of double diffusion and salt fingers in the region, we estimate thermal and haline diffusivities in the salt-finger regime and the resultant heat and salt fluxes using both the empirical relation of Radko and Smith (2012), which depends on the density ratio, R_{ρ} , and the relation of Osborn and Cox (1972), which depends on the rate of destruction of temperature variance, χ . Fluxes estimated using the relation of Radko and Smith (2012) are higher than those estimated using the relation of Osborn and Cox (1972). Nevertheless, turbulent and salt-finger fluxes are small, and their influence on hydrography is likely limited.

Code availability. The MATLAB toolbox of Scheifele et al. (2018) to calculate turbulent kinetic energy dissipation rate following the Batchelor spectrum method is available at https://github.com/bscheife/turbulence_temperature.

Data availability. Standard hydrographic observations from SG620 (Rollo, 2021) are available from the British Oceanographic Data Centre at <https://doi.org/10.5285/c596cdd7-c709-461a-e053-6c86abc0c127>. Processed turbulent kinetic energy dissipation rate estimates (Rollo et al., 2023), from both Batchelor and Thorpe scale methods, are available from the British Oceanographic Data Centre at <https://doi.org/10.5285/f173b9c1-bb50-0b75-e053-6c86abc02a4a>.

Author contributions. PMFS and GMD calculated turbulent kinetic energy dissipation rate following the Batchelor spectrum method. PJL calculated turbulent kinetic energy dissipation rate following the Thorpe scale method. All authors contributed to the analysis. PMFS wrote the paper with assistance from GMD and PJL, and with comments and feedback from KJH and RAH.

Competing interests. The contact author has declared that none of the authors has any competing interests.

Disclaimer. Publisher's note: Copernicus Publications remains neutral with regard to jurisdictional claims in published maps and institutional affiliations.

Acknowledgements. We thank Beth Siddle, Callum Rollo, and the crew and scientists of the RV *Meteor* (cruise M161) for assistance in the deployment and recovery of the glider. We thank Gareth Lee and Marcos Cobas-Garcia for the preparation of the glider and the UEA glider group for piloting. We are indebted to two anonymous reviewers, whose feedback has greatly improved this paper.

Financial support. This research has been supported by the European Research Council (grant no. 741120) and UK Research and Innovation (grant no. NE/N012070/1).

Review statement. This paper was edited by Katsuro Katsumata and reviewed by two anonymous referees.

References

- Batchelor, G. K.: Small-scale variation of convective quantities like temperature in a turbulence fluid. Part one: general discussion and the case of small conductivity, *J. Fluid Mech.*, 5, 113–133, 1959.
- Creed, E., Ross, W., Lueck, R., Stern, P., Douglas, W., Wolk, F., and Hall, R. A.: Integration of an RSI microstructure sensing package into a Seaglider, *Oceans 2015 – MTS/IEEE Washington*, <https://doi.org/10.23919/OCEANS.2015.7404477>, 2015.
- Dillon, T. M.: Vertical overturns: A comparison of Thorpe and Ozmidov scales, *J. Geophys. Res.*, 87, 9601–9631, 1982.
- Fer, I., Nandi, P., Holbrook, W. S., Schmitt, R. W., and Páramo, P.: Seismic imaging of a thermohaline staircase in the western tropical North Atlantic, *Ocean Sci.*, 6, 621–631, <https://doi.org/10.5194/os-6-621-2010>, 2010a.
- Fer, I., Skogseth, R., and Geyer, F.: Internal waves and mixing in the marginal ice zone near the Yermak Plateau, *J. Phys. Oceanogr.*, 40, 1613–1630, 2010b.
- Fer, I., Peterson, A. K., and Ullgren, J. E.: Microstructure measurements from an underwater glider in the turbulent Fareo Bank Channel overflow, *J. Atmos. Ocean. Tech.*, 31, 1128–1150, 2014.
- Fernández-Castro, B., Mouriño-Carballido, B., Benítez-Barrios, V. M., Chouciño, P., Fraile-Nuez, E., Graña, R., Piedeleu, M., and Rodríguez-Santana, A.: Microstructure turbulence and diffusivity parameterisation in the tropical and subtropical Atlantic, Pacific and Indian Oceans during the Malaspina 2010 expedition, *Deep-Sea Res. Pt. I*, 94, 15–30, 2014.
- Frajka-Williams, E., Eriksen, C. C., Rhines, P. B., and Harcourt, R. R.: Determining vertical water velocities from Seaglider, *J. Atmos. Ocean. Tech.*, 28, 1641–1656, 2011.
- Frajka-Williams, E., Brearley, J. A., Nash, J. D., and Whalen, C. B.: New technological frontiers in ocean mixing, in: *Ocean mixing: drivers, mechanisms and impacts*, edited by: Meredith, M. P. and Naveira Garabato, A. C., Elsevier Science, Amsterdam, the Netherlands, <https://doi.org/10.1016/B978-0-12-821512-8.00021-9>, 2021.
- Garau, B., Ruiz, S., Zhang, W. G., Pascual, A., Heslop, E., Kerfoot, J., and Tintoré, J.: Thermal lag correction on Slocum CTD glider data, *J. Atmos. Ocean. Tech.*, 28, 1065–1071, 2011.
- George, J. V., Vinayachandran, P. N., and Nayak, A. A.: Enhanced double-diffusive salt flux from the high-salinity core of Arabian Sea-origin waters to the Bay of Bengal, *J. Phys. Oceanogr.*, 51, 505–518, 2021.
- Howatt, T., Waterman, S., and Ross, T.: On using the finescale parameterisation and Thorpe scales to estimate turbulence from glider data, *J. Atmos. Ocean. Tech.*, 38, 1187–1204, 2021.
- Ijichi, T. and Hibiya, T.: Observed variations in turbulent mixing efficiency in the deep ocean, *J. Phys. Oceanogr.*, 48, 1815–1830, 2018.
- Kelley, D. E., Fernando, H. J. S., Gargett, A. E., Tanny, J., and Özsoy, E.: The diffusive regime of double-diffusive convection, *Prog. Oceanogr.*, 56, 461–481, 2003.
- Lueck, R. G., Wolk, F., and Yamazaki, H.: Oceanic velocity microstructure measurements in the 20th century, *J. Oceanogr.*, 58, 153–174, 2002.
- Mater, B. D., Venayagamoorthy, S. K., St Laurent, L., and Moum, J. N.: Biases in Thorpe-scale estimates of turbulence dissipation. Part 1: assessments from large-scale overturns in oceanographic data, *J. Phys. Oceanogr.*, 45, 2497–2521, 2015.
- Naveira Garabato, A. C., Polzin, K. L., Ferrari, R., Zika, J. D., and Forryan, A.: A microscale view of mixing and overturning across the Antarctic Circumpolar Current, *J. Phys. Oceanogr.*, 46, 233–254, 2016.
- Oakey, N. S.: Determination of the rate of dissipation of turbulent energy from simultaneous temperature and velocity shear microstructure measurements, *J. Phys. Oceanogr.*, 12, 256–271, 1982.
- Osborn, T. R.: Estimates of the local rate of vertical diffusion from dissipation measurements, *J. Phys. Oceanogr.*, 10, 83–89, 1980.
- Osborn, T. R. and Cox, C. S.: Oceanic fine structure, *Geophys. Fluid Dynam.*, 3, 321–345, 1972.
- Ozmidov, R. V.: On the turbulent exchange in a stably stratified ocean, *Atmos. Ocean. Phys.*, 8, 853–860, 1965.
- Palmer, M. R., Stephenson, G. R., Inall, M. E., Balfour, C., Düsterhus, A., and Green, J. A. M.: Turbulence and mixing by internal waves in the Celtic Sea determined from ocean glider microstructure measurements, *J. Marine Syst.*, 144, 57–69, 2015.
- Peterson, A. K. and Fer, I.: Dissipation measurements using temperature microstructure from an underwater glider, *Methods in Oceanography*, 10, 44–69, 2014.
- Polzin, K. L., Naveira Garabato, A. C., Huussen, T. N., Sloyan, B. M., and Waterman, S.: Finescale parameterizations of tur-

- bulent dissipation, *J. Geophys. Res.-Oceans*, 119, 1383–1419, 2014.
- Radko, T.: What determines the thickness of layers in a thermohaline staircase?, *J. Fluid Mech.*, 523, 79–98, 2005.
- Radko, T. and Smith, P. D.: Equilibrium transport in double-diffusive convection, *J. Fluid Mech.*, 690, 5–27, 2012.
- Rainville, L., Gobat, J. L., Lee, C. M., and Shilling, G. B.: Multi-month dissipation estimates using microstructure from autonomous underwater gliders. Multi-month dissipation estimates using microstructure from autonomous underwater gliders, *Oceanography*, 30, 49–50, 2017.
- Rollo, C.: Physical and biogeochemical data from three Seagliders on a combination transect and virtual mooring deployment, NE of Barbados January–February 2020, British Oceanographic Data Centre, National Oceanography Centre, NERC [data set], <https://doi.org/10.5285/c596cdd7-c709-461a-e053-6c86abc0c127>, 2021.
- Rollo, C., Heywood, K. J., and Hall, R. A.: Glider observations of thermohaline staircases in the tropical North Atlantic using an automated classifier, *Geosci. Instrum. Method. Data Syst.*, 11, 359–373, <https://doi.org/10.5194/gi-11-359-2022>, 2022.
- Rollo, C., Siddle, E., Lee, G. A., Cobas-Garcia, M., Sheehan, P. M. F., Leadbitter, P. J., Damerell, G. M., Hall, R. A., and Heywood, K. J.: Estimates of turbulent kinetic energy dissipation rate in the western tropical Atlantic, northeast of Barbados (January and February 2020) calculated from Seaglider temperature microstructure observations using Batchelor spectrum and Thorpe scale methods (R/V Meteor cruise M161), British Oceanographic Data Centre, National Oceanography Centre, NERC [data set], <https://doi.org/10.5285/f173b9c1-bb50-0b75-e053-6c86abc02a4a>, 2023.
- Ruddick, B., Anis, A., and Thompson, K.: Maximum likelihood spectral fitting: the Batchelor spectrum, *J. Atmos. Ocean. Tech.*, 17, 1541–1555, 2000.
- Scheifele, B., Waterman, S., Merkelbach, L., and Carpenter, J. R.: Measuring the dissipation rate of turbulence kinetic energy in strongly stratified, low-energy environments: a case study from the Arctic Ocean, *J. Geophys. Res.-Oceans*, 123, 5459–5480, <https://doi.org/10.1029/2017JC013731>, 2018 (code available at: https://github.com/bscheife/turbulence_temperature, last access: 17 January 2023).
- Schmitt, R. W.: Mixing in a thermohaline staircase, in: Small-scale turbulence and mixing in the ocean, Proceedings of the 19th International Liège Colloquium on ocean hydrodynamics, edited by: Nihoul, J. C. J. and Jamart, B. M., 435–452, Elsevier, Amsterdam, the Netherlands, [https://doi.org/10.1016/S0422-9894\(08\)70563-4](https://doi.org/10.1016/S0422-9894(08)70563-4), 1988.
- Schmitt, R. W., Perkins, H., Boyd, J. D., and Stalcup, M. C.: C-SALT: an investigation of the thermohaline staircase in the western tropical North Atlantic, *Deep-Sea Res.*, 34, 1655–1665, 1987.
- Schmitt, R. W., Ledwell, J. R., Montgomery, E. T., Polzin, K. L., and Toole, J. M.: Enhanced diapycnal mixing by salt fingers in the thermocline of the tropical Atlantic, *Science*, 308, 685–688, 2005.
- Schultze, L. K. P., Merkelbach, L. M., and Carpenter, J. R.: Turbulence and mixing in a shallow shelf sea from underwater gliders, *J. Geophys. Res.-Oceans*, 122, 9029–9109, 2017.
- Scott, R. M., Brearley, J. A., Naveira Garabato, A. C., Venables, H. J., and Meredith, M. P.: Rates and mechanisms of turbulent mixing in a coastal embayment of the West Antarctic Peninsula, *J. Geophys. Res.-Oceans*, 126, e2020JC016861, <https://doi.org/10.1029/2020JC016861>, 2021.
- Sheen, K. L., Brearley, J. A., Naveira Garabato, A. C., Smeed, D. A., Waterman, S., Ledwell, J. R., Meredith, M. P., St Laurent, L., Thurnherr, A. M., Toole, J. M., and Watson, A. J.: Rates and mechanisms of turbulent dissipation and mixing in the Southern Ocean: results from the Diapycnal and Isopycnal Mixing Experiment in the Southern Ocean (DIMES), *J. Geophys. Res.-Oceans*, 118, 2774–2792, 2013.
- Smyth, W. D., Moum, J. N., and Caldwell, D. R.: The efficiency of mixing in turbulent patches: inferences from direct simulations and microstructure observations, *J. Phys. Oceanogr.*, 31, 1969–1992, 2001.
- Sommer, T., Carpenter, J. R., Schmid, M., Lueck, R. G., and Wüest, A.: Revisiting microstructure sensor responses with implications for double-diffusive fluxes, *J. Atmos. Ocean. Tech.*, 30, 1907–1923, 2013.
- St Laurent, L. and Schmitt, R. W.: The contribution of salt fingers to vertical mixing in the North Atlantic Tracer Release Experiment, *J. Phys. Oceanogr.*, 29, 1404–1424, 1999.
- Stevens, B., Bony, S., Farrell, D., Ament, F., Blyth, A., Fairall, C., Karstensen, J., Quinn, P. K., Speich, S., Acquistapace, C., Aemisegger, F., Albright, A. L., Bellenger, H., Bodenschatz, E., Caesar, K.-A., Chewitt-Lucas, R., de Boer, G., Delanoë, J., Denby, L., Ewald, F., Fildier, B., Forde, M., George, G., Gross, S., Hagen, M., Hausold, A., Heywood, K. J., Hirsch, L., Jacob, M., Jansen, F., Kinne, S., Klocke, D., Kölling, T., Konow, H., Lothon, M., Mohr, W., Naumann, A. K., Nuijens, L., Olivier, L., Pincus, R., Pöhlker, M., Reverdin, G., Roberts, G., Schnitt, S., Schulz, H., Siebesma, A. P., Stephan, C. C., Sullivan, P., Touzé-Peiffer, L., Vial, J., Vogel, R., Zuidema, P., Alexander, N., Alves, L., Arixi, S., Asmath, H., Bagheri, G., Baier, K., Bailey, A., Baranowski, D., Baron, A., Barrau, S., Barrett, P. A., Batier, F., Behrendt, A., Bendinger, A., Beucher, F., Bigorre, S., Blades, E., Blossey, P., Bock, O., Böing, S., Bosser, P., Bourras, D., Bouruet-Aubertot, P., Bower, K., Branellec, P., Branger, H., Brennek, M., Brewer, A., Brilouet, P.-E., Brüggemann, B., Buehler, S. A., Burke, E., Burton, R., Calmer, R., Canonici, J.-C., Carton, X., Cato Jr., G., Charles, J. A., Chazette, P., Chen, Y., Chilinski, M. T., Choularton, T., Chuang, P., Clarke, S., Coe, H., Cornet, C., Coutris, P., Couvreur, F., Crewell, S., Cronin, T., Cui, Z., Cuypers, Y., Daley, A., Damerell, G. M., Dauhut, T., Deneke, H., Desbios, J.-P., Dörner, S., Donner, S., Douet, V., Drushka, K., Dütsch, M., Ehrlich, A., Emanuel, K., Emmanouilidis, A., Etienne, J.-C., Etienne-Leblanc, S., Faure, G., Feingold, G., Ferrero, L., Fix, A., Flamant, C., Flatau, P. J., Foltz, G. R., Forster, L., Furtuna, I., Gadian, A., Galewsky, J., Gallagher, M., Gallimore, P., Gaston, C., Gentemann, C., Geyskens, N., Giez, A., Gollop, J., Gouirand, I., Gourbeyre, C., de Graaf, D., de Groot, G. E., Grosz, R., Güttler, J., Gutleben, M., Hall, K., Harris, G., Helfer, K. C., Henze, D., Herbert, C., Holanda, B., Ibanez-Landeta, A., Intrieri, J., Iyer, S., Julien, F., Kalesse, H., Kazil, J., Kellman, A., Kidane, A. T., Kirchner, U., Klingebiel, M., Körner, M., Kremper, L. A., Kretschmar, J., Krüger, O., Kumala, W., Kurz, A., L'Hégaret, P., Labaste, M., Lachlan-Cope, T., Laing, A., Landschützer, P., Lang, T., Lange, D., Lange, I., Laplace, C., Lavik,

- G., Laxenaire, R., Le Bihan, C., Leandro, M., Lefevre, N., Lena, M., Lenschow, D., Li, Q., Lloyd, G., Los, S., Losi, N., Lovell, O., Luneau, C., Makuch, P., Malinowski, S., Manta, G., Marinou, E., Marsden, N., Masson, S., Maury, N., Mayer, B., Mayers-Als, M., Mazel, C., McGeary, W., McWilliams, J. C., Mech, M., Mehlmann, M., Meroni, A. N., Mieslinger, T., Minikin, A., Minnett, P., Möller, G., Morfa Avalos, Y., Muller, C., Musat, I., Napoli, A., Neuberger, A., Noisel, C., Noone, D., Nordsiek, F., Nowak, J. L., Oswald, L., Parker, D. J., Peck, C., Person, R., Philippi, M., Plueddemann, A., Pöhlker, C., Pörtge, V., Pöschl, U., Pologne, L., Posyniak, M., Prange, M., Quiñones Meléndez, E., Radtke, J., Ramage, K., Reimann, J., Renault, L., Reus, K., Reyes, A., Ribbe, J., Ringel, M., Ritschel, M., Rocha, C. B., Rochetin, N., Röttenbacher, J., Rollo, C., Royer, H., Sadoulet, P., Saffin, L., Sandiford, S., Sandu, I., Schäfer, M., Schemann, V., Schirmacher, I., Schlenczek, O., Schmidt, J., Schröder, M., Schwarzenboeck, A., Sealy, A., Senff, C. J., Serikov, I., Shohan, S., Siddle, E., Smirnov, A., Späth, F., Spooner, B., Stolla, M. K., Szkółka, W., de Szoeko, S. P., Tarot, S., Tetoni, E., Thompson, E., Thomson, J., Tomassini, L., Totems, J., Ubele, A. A., Villiger, L., von Arx, J., Wagner, T., Walther, A., Webber, B., Wendisch, M., Whitehall, S., Wiltshire, A., Wing, A. A., Wirth, M., Wiskandt, J., Wolf, K., Worbes, L., Wright, E., Wulfmeyer, V., Young, S., Zhang, C., Zhang, D., Ziemann, F., Zinner, T., and Zöger, M.: EUREC⁴A, *Earth Syst. Sci. Data*, 13, 4067–4119, <https://doi.org/10.5194/essd-13-4067-2021>, 2021.
- Taylor, J. R. and Veronis, G.: Experiments on double-diffusive sugar-salt fingers at high stability ratio, *J. Fluid Mech.*, 321, 315–333, 1996.
- Thorpe, S. A.: Turbulence and mixing in a Scottish loch, *Philos. T. R. Soc. S.-A*, 286, 125–181, 1977.
- Thorpe, S. A.: On the shape and breaking of finite amplitude internal gravity waves in a shear flow, *J. Fluid Mech.*, 85, 7–31, 1978.
- Thorpe, S. A.: Measuring overturns with gliders, *J. Marine Res.*, 70, 93–117, 2012.
- van der Boog, C. G., Dijkstra, H. A., Pietrzak, J. D., and Katsman, C. A.: Double-diffusive mixing makes small contribution to the global ocean circulation, *Nature Communications Earth & Environment*, 2, 46, <https://doi.org/10.1038/s43247-021-00113-x>, 2021.
- Whalen, C. B.: Best practices for comparing ocean turbulence measurements across spatiotemporal scales, *J. Atmos. Ocean. Tech.*, 38, 837–841, 2021.
- Whalen, C. B., Talley, L. D., and MacKinnon, J. A.: Spatial and temporal variability of global ocean mixing inferred from Argo profiles, *Geophys. Res. Lett.*, 39, L18612, <https://doi.org/10.1029/2012GL053196>, 2012.
- Whalen, C. B., MacKinnon, J. A., Talley, L. D., and Waterhouse, A. F.: Estimating the mean diapycnal mixing using a finescale parameterisation, *J. Phys. Oceanogr.*, 45, 1174–1188, 2015.